Chapter-3

Oxygen reduction reaction in a Ruddlesden-Popper perovskite (SmSr)$NiO_{4-\delta}$

Publication*: M. Chauhan, P. K. Jha, A. S. Bangwal, P. A. Jha and P. Singh*, **"Microstructural dependent oxygen reduction in a Ruddlesden-Popper perovskite $SmSrNiO_{4-\delta}$"** *Phys. Chem. Chem. Phys., vol. 21, no. 27, pp. 1 2020, 22, 12294, doi: 10.1039/D0CP00433B.*

CHAPTER 3: Oxygen reduction reaction in a Ruddlesden-Popper perovskite $SmSrNiO_{4-\delta}$

3.1 Introduction

The quest for suitable energy materials for the various components of these cells and batteries is a much focused-on area of research. Perovskite Mott insulators and their derivatives, which undergo an insulator to metal transition at room temperature and above, have attracted the interest of the researchers community due to their potential use as electrodes[127]–[130]. To enhance the efficiency of fuel cells, typically solid oxide fuel cells, fast oxygen reduction reaction (ORR) at the cathode is required[131]. Recently, hydrogenated $SmNiO_3$ has been proposed as an electrolyte material for SOFCs, which operates by blocking the electron transfer between degenerated d-orbitals[132]. Ruddlesden-Popper (RP) layered structured materials have been proved to be good electrolyte materials for SOFCs. In addition, a RP-based nickelate series ($Ln_{n+1}Ni_nO_{3n+1}$; n=1), have gained much attention as an alternative cathode material[133], [134], because of observed large oxide-ion conductivity coupled with reasonable electrical conductivity[135].

The faster oxygen surface kinetics in the RP materials extends the electrochemically active region to the entire oxygen surface and minimizes the triple phase boundary[136]. The ORR kinetics in case of RP structures Is not well understood. Rather, effect of substitution of cations on A-site and B-site have not been discussed. Furthermore, dense microstructures allow different oxygen transport kinetics, as an increase in polarization resistance and lower density of grain boundaries minimizes ORR. In addition, morphology changes influence catalytic activity by changing the mass transfer efficiency[137].

'Ni' is a strong catalytic transition metal, the use of which brings about some issues such as corrosion and stability under oxidizing/reducing conditions that hinder its application as an electrode material[138], [139]. Corrosion decreases the performance of fuel cells and can also limit the life of fuel cells. The rate of corrosion mainly depends upon the electrode material, electrolyte used and the operating temperature, where it is observed to increase with an increase in the temperature. Furthermore, Pourbaix[140] first used potential-PH diagrams to discuss the corrosion and dissolution of the metal electrodes in aqueous solution. Simultaneously, the corrosion of palladium and platinum were also studied using electrocatalysis at potentials of the oxygen layer and oxygen evolution regions[141]. In addition, the disintegration of electrodes due to strain and degradation of the bonding material (to form complexes) have not been dealt with so far.

The microstructural design of electrode materials plays an important role, not only in electron and oxygen ion conduction at the electrolyte-electrode and electrode-air interfaces (ORR) but also on the life time of fuel cells. Ni-based compounds with enhanced oxygen ion conductivity can be used as a buffer (interfacial layer between electrolyte- electrode) or even as an electrolyte, where direct exposure to reducing conditions can be avoided.

Hence, in the view of the above in this chapter, $(SmSr)NiO_{4-\delta}$ with porous and pore-free microstructures were prepared *via* a solid-state synthesis route and the influence of catalysis on the structure after Voltammetry was comprehensively studied. In addition, the corrosion rate, corrosion voltage and current were also estimated using Tafel plots.

3.2 Methodology

3.2.1 Sample preparation

$SmSrNiO_{4-\delta}$ ceramic samples were prepared *via* a conventional solid-state reaction process using 6.559 g of samarium oxide (Sm_2O_3) (M/s CDH with a purity of 99.9%), 5.604 g of Strontium carbonate ($SrCO_3$) (M/s CDH with purity 99%), and 2.836 g Nickel Oxide (NiO) (M/s Alfa Aesar with purity 99%) which were weighed and wet ground in an acetone medium for 2 h followed by dry grinding for 2 h in an agate mortar. The powder was then used for Thermogravimetric (TGA) measurements by Metler Toledo DTA instrument. The composition was calcined at 1200 ˚C for 3h at a heating rate of 5 ℃ min^{-1}. The calcined powder was then ground again in an agate mortar and mixed with 2% polyvinyl alcohol (PVA) as a binder and thereafter pelletized using a hydraulic pellet press by applying uniaxial pressure of 5 tons. The pellets were pre-heated in an oven at 300 ºC (at a heating rate of 5 ℃ min^{-1}) and finally sintered at 1250, 1300, 1350, 1400 and 1425 ºC for 3h at a heating rate of 5˚/min. the amount of powder used to prepare the pellets was ~1 g.

3.2.2 Characterization techniques

The TGA measurements were performed under two different atmospheres, Oxygen and Nitrogen at a heating rate of 5 ˚C min^{-1} to study the weight loss of the sintered powders using a Mettler Toledo (Germany) instrument. The phase purity of the samples was determined *via* powder x-ray diffraction (PXRD, Rigaku Miniflex II desktop) using Cu-Kα radiation (λ ~ 1.4506 Å) at room temperature in the 2θ range 20º-70º with a step of 0.01º with the scanning rate of 2 º/minute. The density of the sintered pellets was measured by Archimedes m 3ethod with a Denver Kit. The Fourier Transform infrared (FTIR) spectroscopy was performed

via Nicolet iS5 using Attenuated Total Reflection (ATR) mode over the spectral range of 400 to 4000 cm^{-1}. The Surface morphology was analyzed using scanning electron microscopy (Nova Nano SEM 450). The high-temperature transient current response was recorded using a Keithley 6517B electrometer/High resistance meter. The electrochemical performance was studied by cyclic voltammetry (CV), carried out using a potentiostat/galvanostat (μAutolab type III from Metrohm) equipped with a three-electrode electrochemical system, where Ag/AgCl were used as a reference electrode, Pt wire as a counter electrode and samples sintered at 1250 and 1425 °C were used as the working electrodes with 0.1 M Na_2SO_4 solution used as an electrolyte. Before starting the measurements, the open circuit voltage was stabilized for 15 minutes, after which a stabilized V_{OC} value was obtained and then different scans were carried out.

3.3 Result and discussion

3.3.1 Structural details of the calcined powder

The RP-structured layered perovskite $(SmSr)NiO_{4-\delta}$ is processed using a conventional solid-state reaction. The calcination temperature was optimized at 1200 °C using TGA measurements (Fig.3.1(a)). The TGA analysis performed up to 1000 °C revealed the weight loss after 840 °C, which infers the formation of the $SmSrNiO_{4-\delta}$ compound after 840 °C. In addition, a kink is also observed at 278 °C, indicating removal of CO instead of CO_2 depicted through weight loss percentage according to the following reaction (3.1).

$$Sm_2O_3 + 2SrCO_3 + 2NiO \rightarrow 2(SmSr)NiO_{4-\delta} + 2CO + \frac{1+\delta}{2} O_2 \quad (3.1)$$

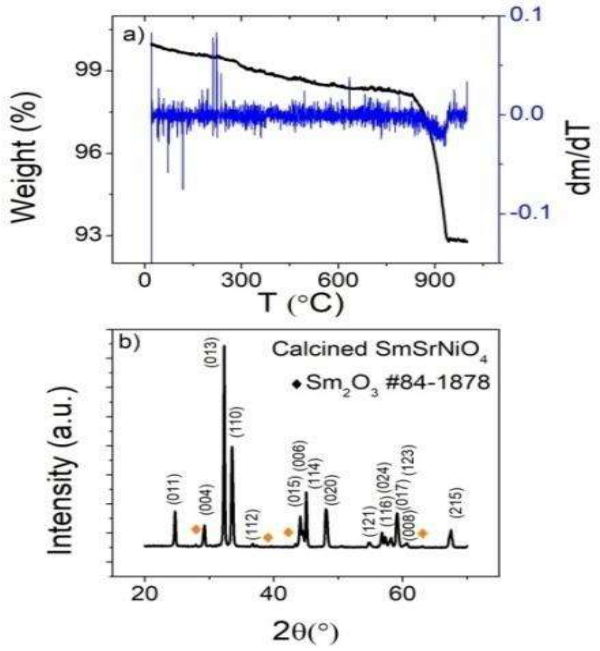

Figure 3.1: (a) TGA, DTGA of raw powder and (b) XRD of calcined powder $SmSrNiO_{4-\delta}$

Further, differential thermal analysis is also showing a disturbance around 280 °C and a kink at 840 °C, but after that again, an increase is observed. This rise further corresponds to the oxidation of the sample. Hence, the calcination should be done well above 1000 °C for the proper oxygen content, according to the Ruddlesden Popper phase. Fig.3.1(b) depicts the X-ray diffractogram of the powder calcined at 1200 °C for 3hr and matches well with the tetragonal phase (I4/mmm symmetry) according to JCPDS File No. 480973. The XRD pattern of the calcined powder is refined using Full Prof Suite package with I4/mmm symmetry. The refinement is done using peak profile Thomson Cox Hastings Pseudo Voigt and Axial divergence symmetry along with the instrument parameters, and the refinement factors obtained are $R_f = 3.66$ and Bragg R-factor = 5.66. The lattice parameters obtained are a = b = 3.7786 Å and c =12.2289 Å.

After the nearly single-phase formation of calcined powder as confirmed through Rietveld refinement, the sintering temperature was varied at 1250, 1300, 1350, 1400 and 1425 ˚C (Fig.3.2).

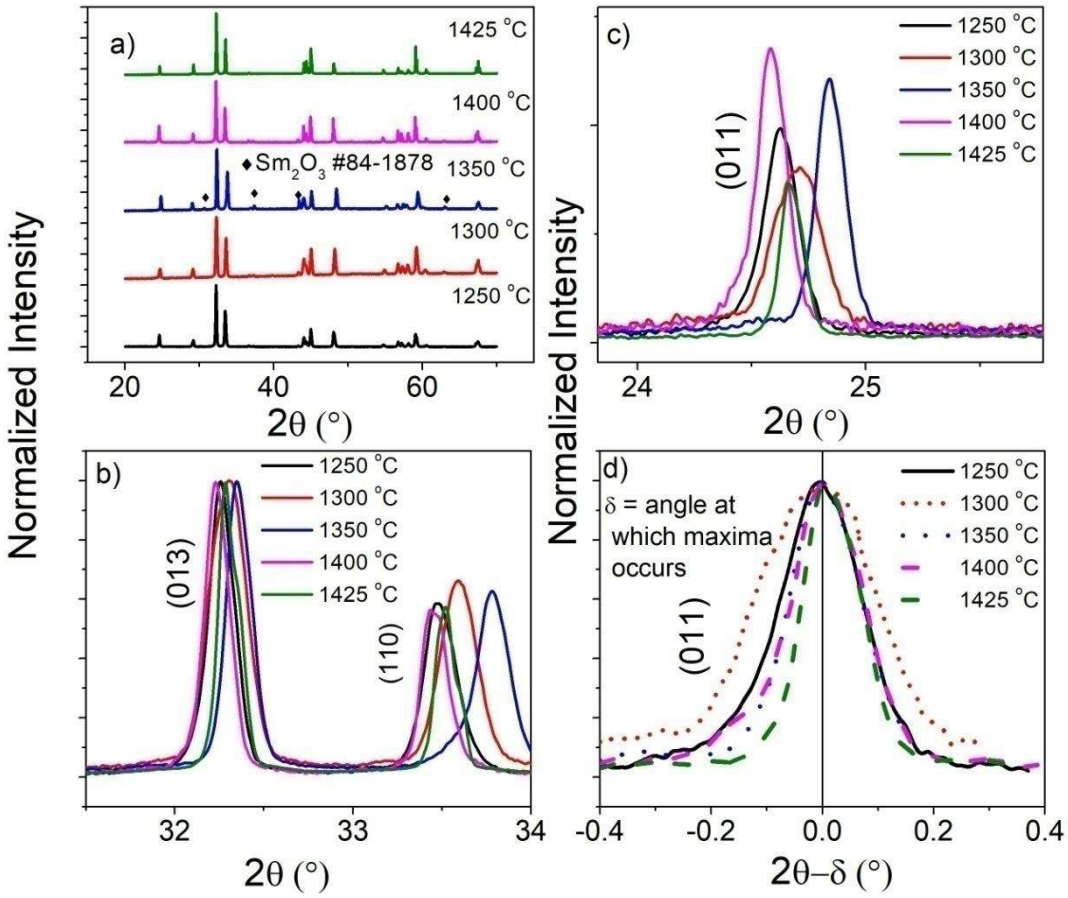

Figure 3.2 (a) XRD pattern of the $SmSrNiO_{4-\delta}$ sample sintered at different sintering temperatures 1250 ˚C, 1300 ˚C, 1350 ˚C, 1400 ˚C, and 1425 ˚C, (b) Shifting and FWHM of the studied samples corresponding to 2θ ~ 32°, (c) Shifting and FWHM of the studied samples corresponding to 2θ ~ 24°, (d) Diffuseness of XRD peak (011) corresponding to 2θ ~ 24°

The XRD of $SmSrNiO_{4-\delta}$ sample sintered at different temperatures reveal the single phase of the samples (Fig.3.2(a)). The secondary phases are observed to occur in the sample sintered at 1350 °C belonging to Sm_2O_3 (JCPDS File No. 84-1878). Fig.3.2(b) and (c) correspond to the peaks (013), (110), and (011) at 2θ ~ 32°, 33°, and 24°, respectively. It can be seen that there

is uniform FWHM for (013) peak instead of (110) and (001) peak. To observe this shifting keenly, diffuseness has been plotted using (011) peak. Fig. 3.2(d) shows the variation of Intensity with 2θ-δ, where δ is the angle where maxima occur. It can be seen that before 1350 ^{o}C, the XRD peaks diffuse towards lower angle while for sintering temperature greater than 1350 ^{o}C, XRD peaks diffuse towards higher angle. The XRD peaks observed here are also seen to possess angle shifting with the sintering and hence, lattice parameter alteration. With increase in the sintering temperature, the lattice parameter 'a' (also b, due to tetragonal phase) is shown in fig.3.2 (c). Interestingly, the variation in the lattice parameter related to the phase purity of the sample (Fig. 3.3(c)).

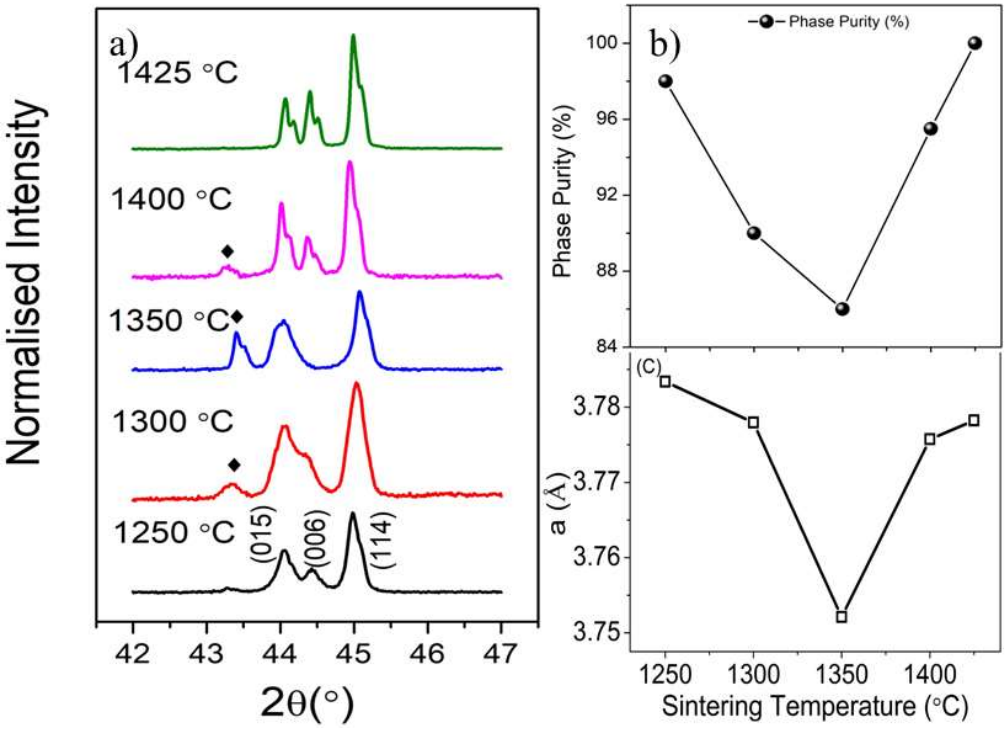

Figure 3.3 (a) X-ray diffractograms of the $SmSrNiO_{4-\delta}$ sample sintered at different sintering temperatures 1250 ˚C, 1300 ˚C, 1350 ˚C, 1400 ˚C, and 1425 ˚C corresponding to 2θ ~ 43° - 46°, (b) Phase purity of the studied samples (c) Variation of lattice parameters with the sintering temperature.

A careful analysis regarding the secondary phase is shown in Fig.3.3(a). The intensity of the secondary phases observed in the calcined powder decreases with the sintering at 1250 ^{o}C, further observed to increase with the increase in sintering temperature up to 1350 ^{o}C and then decreases again with the further rise in sintering temperature. Hence, the phase purity of all the samples is determined using $\varphi_{purity} = \frac{I_p}{I_p + 0.8\, I_s}$, I_p is the maximum intensity of primary peak and I_S is the maximum intensity of the secondary phase. Fig.3.3(b) shows that the phase purity is minimum for the sample sintered at 1350 ^{o}C and maximum at 1425 ^{o}C (~100%). It is observed that the phase purity decreases in line with the sintering temperature up to 1350 °C, and thereafter we observed a phase pure sample after sintering at 1425 °C. Beyond this temperature, the sample starts to melt. The XRD pattern of the sintered samples were refined with I4/mmm symmetry and peak profile Thomson Cox Hastings Pseudo Voigt and Axial divergence symmetry (Fig.3.4). The Rietveld refined XRD is shown in Fig. 3.4 and the refinement factors lie within the appreciable error range. The atomic positions, occupancy, and R-factors are listed in the table 3.1 for the ready reference. From structural results, it can be seen that the sample sintered at 1350 ^{o}C is highly impure.

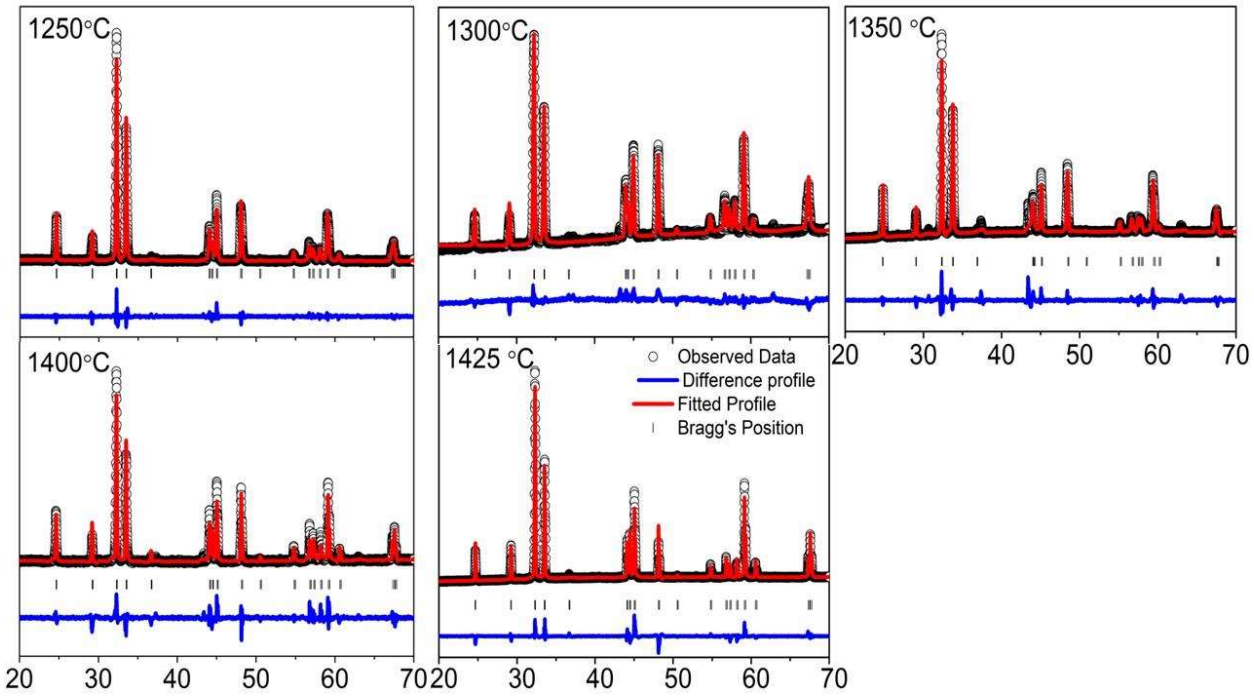

Figure 3.4 Rietveld refined X-ray diffractograms of the $SmSrNiO_{4-\delta}$ sample sintered at different sintering temperatures 1250 ˚C, 1300 ˚C, 1350 ˚C, 1400 ˚C, and 1425 ˚C. The figure contains the data points, intensity obtained, difference profiles and Bragg positions of the samples sintered at different temperatures.

Sample	Sintering Temperature (°C)	Atoms	Position coordinates			Occupancy	B (Å^2)	R-factors	
			x	y	z			R_{wp}	Re
T1	1250	Sm	0	0	0.36342	1	0.7441	9.97	6.51
		Sr	0	0	0.36342	1	0.9600		
		Ni	0	0	0	1	0.8133		
		O1	0	0.5	0	1	0.4730		
		O2	0	0	0.10	1	0.4970		
T2	1300	Sm	0	0	0.36355	1	0.6367	11.8	7.11
		Sr	0	0	0.36355	1	0.9423		
		Ni	0	0	0	1	0.7534		
		O1	0	0.5	0	1	0.4647		
		O2	0	0	0.10	1	0.4588		
T3	1350	Sm	0	0	0.36160	1	0.6339	11.3	5.70
		Sr	0	0	0.36160	1	0.9467		
		Ni	0	0	0	1	0.7556		
		O1	0	0.5	0	1	0.4677		
		O2	0	0	0.10	1	0.4543		

T4	1400	Sm	0	0	0.36476	1	0.6834	11.9	6.67
		Sr	0	0	0.36476	1	0.9634		
		Ni	0	0	0	1	0.7866		
		O1	0	0.5	0	1	0.4933		
		O2	0	0	0.1	1	0.7567		
T5	1425	Sm	0	0	0.36151	1	0.7644	10.1	6.83
		Sr	0	0	0.36151	1	0.9832		
		Ni	0	0	0	1	0.7786		
		O1	0	0.5	0	1	0.4378		
		O2	0	0	0.1	1	0.5647		

Table 3.1: Atomic positions and R-factors obtained after refinement for the $SmSrNiO_{4-\delta}$ samples sintered at different temperature

However, the density measured using the Archimedes method was found to increase with the sintering temperature up to 1400 °C, there-after a slight reduction in density is observed for the sample sintered at 1425 ˚C (Fig. 3.5). Similarly, grain growth was also observed with sintering temperature. The sample sintered at 1250 ˚C is porous with an average grain size ~1.2 μm, while the sample sintered at 1425 ˚C is dense with average grain size > 4μm. However, surface microstructure of the samples is quite different (Fig. 3.6). In addition, grain size is observed to increase with the increase in sintering temperature and is observed as 1.236 μm, 2.659 μm, 2.748 μm and 4.129 μm for the samples sintered at 1250 ˚C, 1300 ˚C, 1350 ˚C, and 1400 ˚C, respectively. The increase in grain size is leading to a reduction in porosity with the increase in sintering temperature. Whereas, the long channel formation on the surface of grains is seen in the sample sintered at 1425 °C (Fig.3.6(e)) as the grains have enlarged enormously (Fig.3.6(e) inset). This is showing the change in surface behavior of the sample sintered at 1425 °C in comparison to 1250 °C. Further, EDX has been studied and showing that at 1400 °C, the sample is highly Ni-rich. Thus, surface behavior may have altered due to Ni.

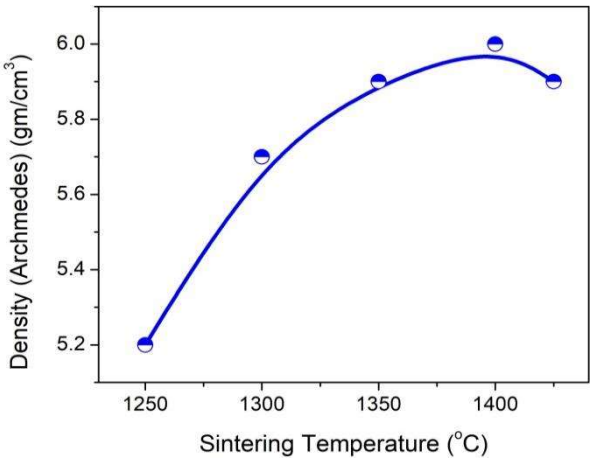

Figure 3.5: Variation of density with the increase in sintering temperature showing a hump at 1400 ^{o}C, proving the optimized sintering temperature.

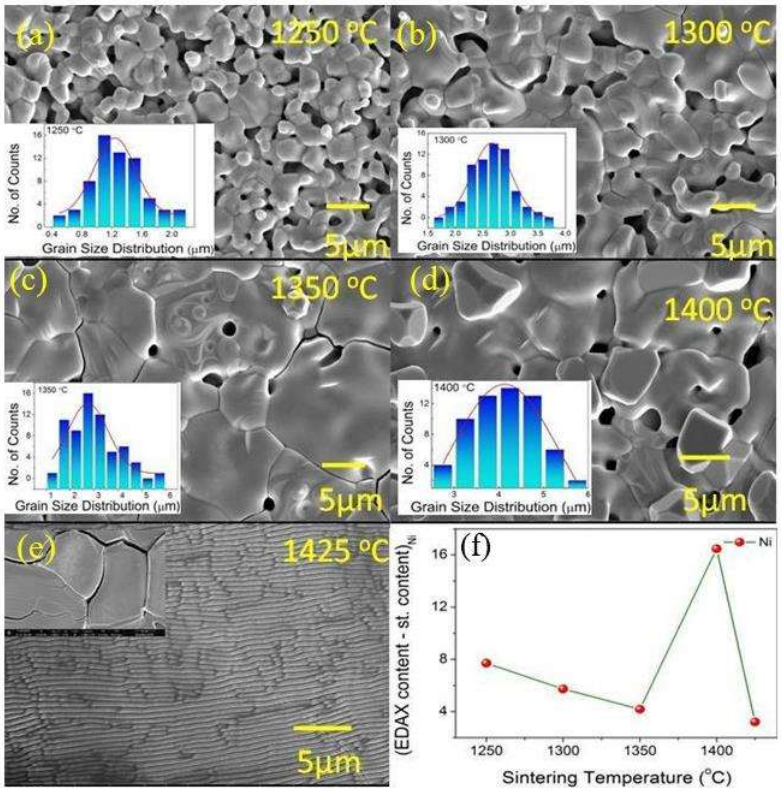

Figure 3.6 (a-e) SEM micrographs of $SmSrNiO_{4-d}$ sample sintered at different sintering temperatures (e) inset surface of the sample sintered at 1425 ^{o}C and (f) Excess Ni measured through EDX of the studied samples.

Recently, we have observed that surface morphology significantly affects the oxide ion conductivity [142] as well as catalytic behaviour[143]. In order to understand the mechanism

behind the oxygen reduction reaction (ORR) process, in the present study, we further investigated the samples sintered at extreme temperatures of 1250 ˚C and 1425 ˚C.

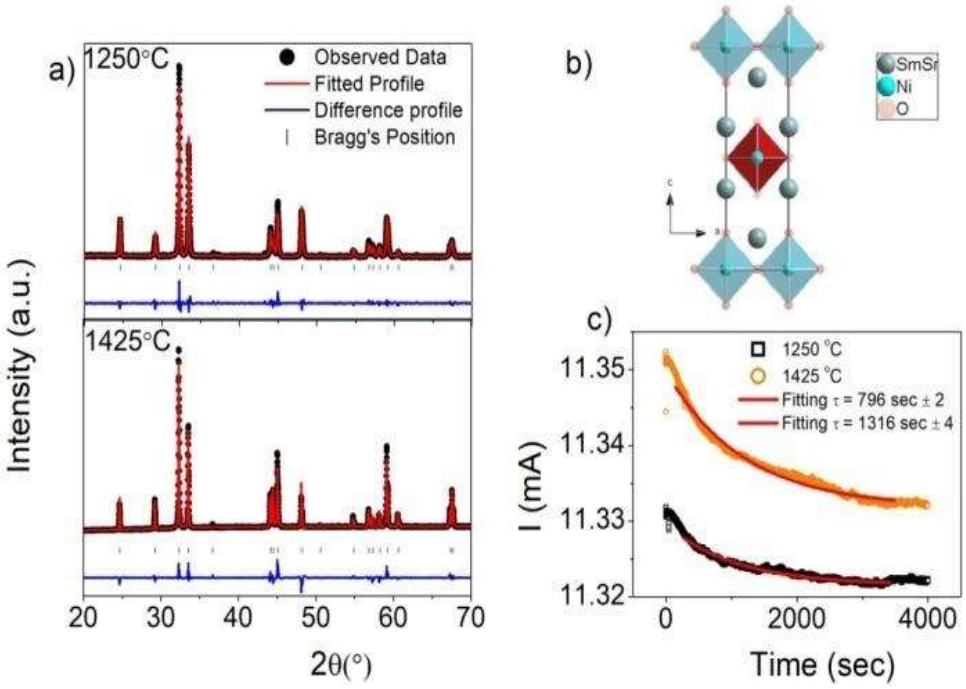

Figure 3.7 (a) Rietveld refinement of X-ray diffractograms of $SmSrNiO_4$ sample sintered at sintering temperatures 1250 ºC and 1425 ºC, respectively, (b) structure obtained from Diamond software using cif files from Rietveld refinement (c) Transient current response along with the exponential fit for the time constant of the sample sintered at sintering temperatures 1250 ºC and 1425 ºC, respectively

The Rietveld refined XRD patterns of the phase pure samples sintered at 1250 and 1425 ºC are presented in Fig.3.7(a). The layered structure is also shown in Fig.3.7(b). The samples are observed to be highly conducting and also, the sample sintered 1425 ºC seems to be more ionic compared to the sample 1250 ºC estimated from the transient current measurements at 700 ºC (transference number) (Fig.3.7(c)). It can be observed from Fig. 3.7(c) that the current begins to decrease gradually with time. The data was fitted using an exponential decay equation to obtain the characteristics relaxation time. A steady current is achieved at 796 sec and 1316 sec,

respectively for the samples sintered at 1250 and 1425 °C. This shows an increase in oxygen vacancies with the sintering temperature (the samples are oxygen deficient).

For the detection of relative Oxygen content, we used the thermogravimetric analysis (TGA). The relative oxygen content estimated from the TGA analysis for the samples sintered at 1250 ˚C and 1425 ˚C is shown in Table 3.2. Although Oxygen is light atom, hence it cannot be calculated accurately from TGA, but it can be roughly estimated. For this purpose, the roughly estimated values of relative oxygen content using TGA is tabulated in Table 3.2.

	Relative Oxygen content, δ	
Sample Sintered at	TGA N_2 (inert) atm	TGA O_2atm
1250 °C	+0.707	-0.704
1425 °C	+0.706	-0.700

Table 3.2: Relative Oxygen content estimated for $SmSrNiO_{4-\delta}$ from TGA in O_2 and N_2 atmosphere

A weight gain was observed in the TGA measurements of both the samples (sintered at 1250 and 1425 °C) under N_2 atmosphere (Fig. 3.8). This weight gain in a N_2 atmosphere is basically due to buoyancy effect, stoichiometry changes and O_2 impurities in the N_2[144]. In the present case, it is associated with the change in stoichiometry, i.e., change in δ as per the equation. Under an O_2 atmosphere, gradual mass loss was observed with an increase in temperature.

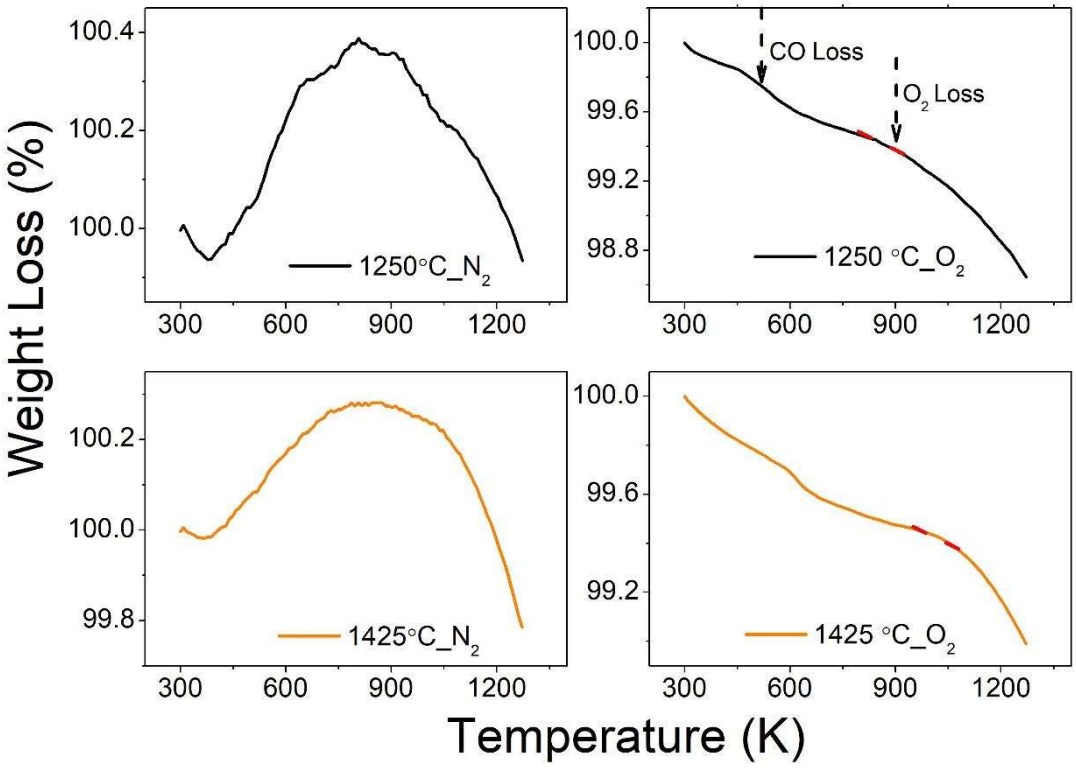

Figure 3.8: TGA of $SmSrNiO_{4-\delta}$ sample sintered at sintering temperatures 1250 ºC and 1425 ºC in N_2 and O_2 atmospheres, respectively

Here, two kinks are observed at ~ 450K and 900K, corresponding to CO and O_2 loss, respectively (as per the weight loss predicted using the above eqn (3.1)). The kink observed at ~ 900 K was used to estimate the oxygen content and is listed in Table 1 for both samples[144]. Hence, it can be concluded that under N_2 atmosphere, the samples are O_2 deficient. However, under an O_2 atmosphere, the samples become oxygen rich. This may be due to oxygen adsorbed at interstitial sites in the layered structure. It can be concluded from Table 3.2 that the thermal transport behaviour of sample sintered at 1425 °C and 1250 °C does not indicate much difference in the relative oxygen content.

The oxidation behaviour of the two samples was examined to understand the variation in d*m*/dT with temperature under different atmospheres (Fig. 3.9). Here, the peak corresponds to

the decomposition temperature. In the N_2 atmosphere, a peak is observed which is the same in mass loss (Fig. 3.8) and dm/dT curves (Fig.3.9) (highlighted in the cyan region). Furthermore, in the O_2 atmosphere, the two kinks observed correspond to the peaks in the dm/dT curves (marked by black arrows). This decomposition temperature, observed to split in two peaks under an O_2 atmosphere. Also, the sintering temperature was observed to change the peak shape. Normally, it is believed that the oxygen deficiency, δ, increases the structural instability, which leads to incommensurate modifications. Furthermore, these modifications reduce the structural energy and the greater oxygen deficiency leads to the formation of unstable structures[145]. In the present case, the oxygen deficiency is observed to be nearly equal to the sintering temperature and hence, it should not alter the structural energy or the structural stability of the compounds. However, the RP structure is unstable because it has higher oxygen deficiency in comparison to other structures. Furthermore, in terms of the sintering temperature, a very small decrease in the value of the lattice parameter 'a' is observed (Fig.3.3(c)), in correlation with small changes in oxygen deficiency (higher oxygen deficiency leads to lattice shrinkage)[145].

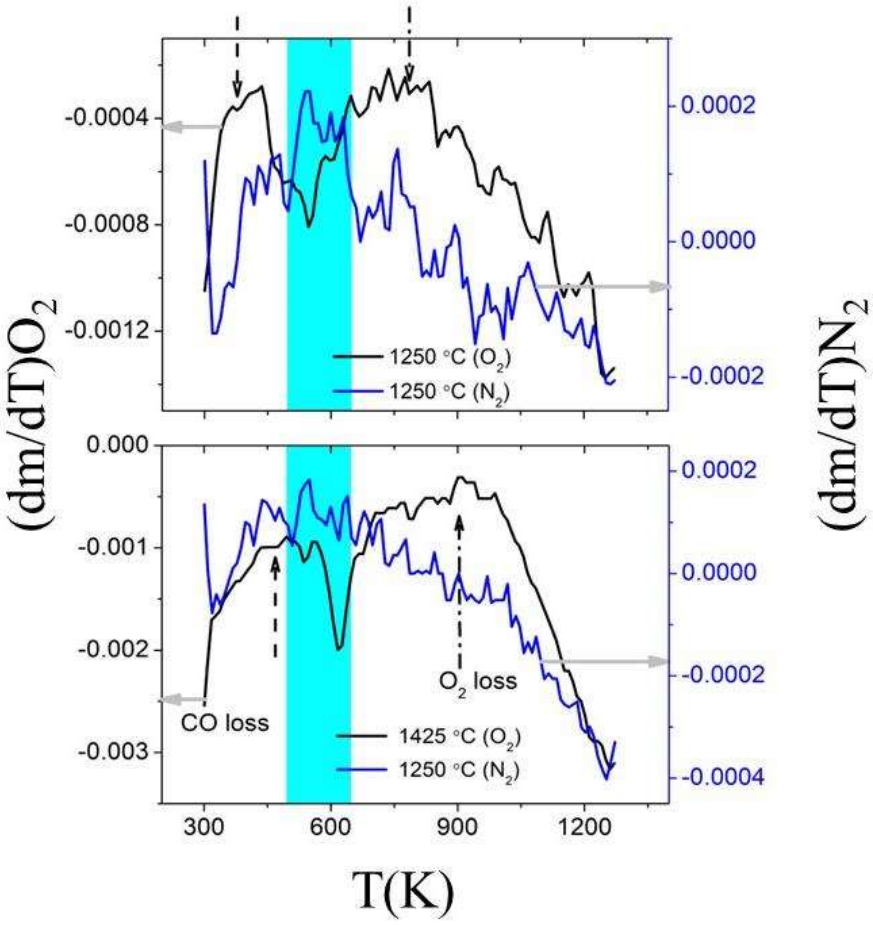

Figure 3.9: The dm/dT values of the $(SmSr)NiO_{4-\delta}$ samples sintered at 1250 and 1425 °C under N_2 and O_2 atmospheres.

To understand the catalytic and redox behaviour, the CVs of both the samples were recorded (Fig 3.10(a)). The catalytic behaviour of the studied samples should be different as it was observed that the sample sintered at 1250 °C has porous morphology (Fig.3.10(b)) and the sample sintered at 1425 °C has pore-free long channels at its surface (Fig. 3.10(c)).

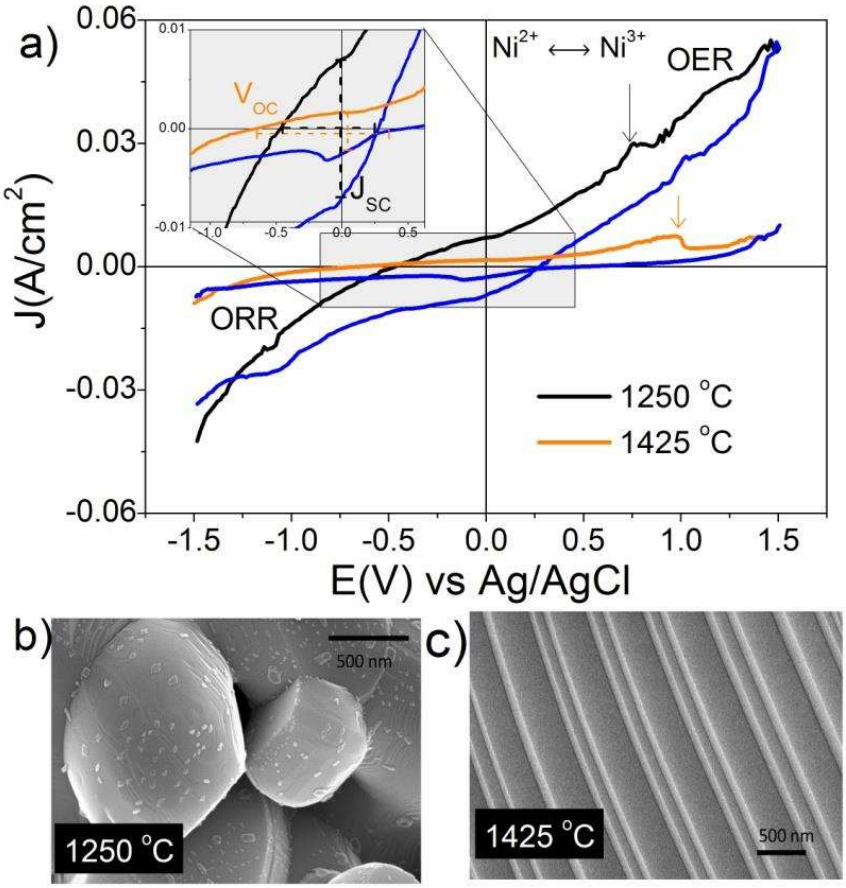

Figure 3.10 (a) Cyclic Voltammetry and (b, c) SEM of $(SmSr)NiO_{4-\delta}$ sample sintered at 1250 °C and 1425 °C, respectively.

It can be observed from Fig. 3.10(a) that the anodic current is higher in the sample sintered at 1250 °C in comparison to the sample sintered at 1425 °C. Simultaneously, the oxygen evolution reaction (OER) is stronger in the sample sintered at 1250 °C compared with the sample sintered at 1425 °C. In addition, the short circuit current is higher in the sample sintered at 1250 °C (~ 4 mA) than that of the current of the 1425 °C (~ 3.7 mA). On a comparative note, the open-circuit voltage (V_{OC}) of the sample sintered at 1425 °C (~1.1 V) is higher than that of the sample sintered at 1250 °C (~0.73). The higher short circuit current value suggests better electrochemical activity in the sample sintered at 1250 °C compared with the sample sintered at 1425 °C sample, suggesting the conversion of Ni^{3+} to Ni^{2+} as the redox reaction takes place:

$$2NiO + \frac{1}{2}\,O_2 \leftrightarrow Ni_2O_3 \qquad (3.2)$$

In the oxygen reduction reaction (ORR), a kink is observed in the pore-free sample, while a kink with reduced intensity is observed in the porous sample. This kink indicated the formation of multiple oxidation states, as suggested earlier in eqn (3.2). In a CV curve, during the OER, the sample loses an electron to become an ion, *e.g.*, $Fc \rightarrow Fc^{+} + e$-, and during the ORR, this process reverses and the ion reduces to the atom. In the present case, this kink indicates the oxidation and reduction of the Ni^{3+} ion. Also, it was observed that the area under the curve for the porous sample is greater than the area under the curve for the pore-free sample. The higher area under the curve indicates a faster ORR/OER mechanism and it also suggests different catalytic mechanisms (different electron/step pathways) for both samples, which will be discussed later. However, the loops observed are quasi-reversible (C_rE_r) in nature indicating that the mechanism can be reversible by electron transfer[122]. Also, the higher the equilibrium constant determined from the voltammograms, the more reversible the voltammograms[146]. In the present case, the CV of the sample sintered at 1250 ℃ is more reversible than that of the sample sintered at 1425℃.

The corrosion rate (CR) can be extracted from the Tafel plots (Fig.3.11) using the equation CR (mm per year) = 3.27 × I_{corr} (mA cm^{-2}) × (ew/d), where ew is the equivalent weight and *d* is density of the material[147]. It can be observed that the CR is lower by one order in magnitude for the sample sintered at 1425 ℃ (~0.0091 mm per year) in comparison to the sample sintered at 1250 ℃ (~ 0.042 mm per year). Thus, the sample sintered at 1425 ℃ corrodes very slowly.

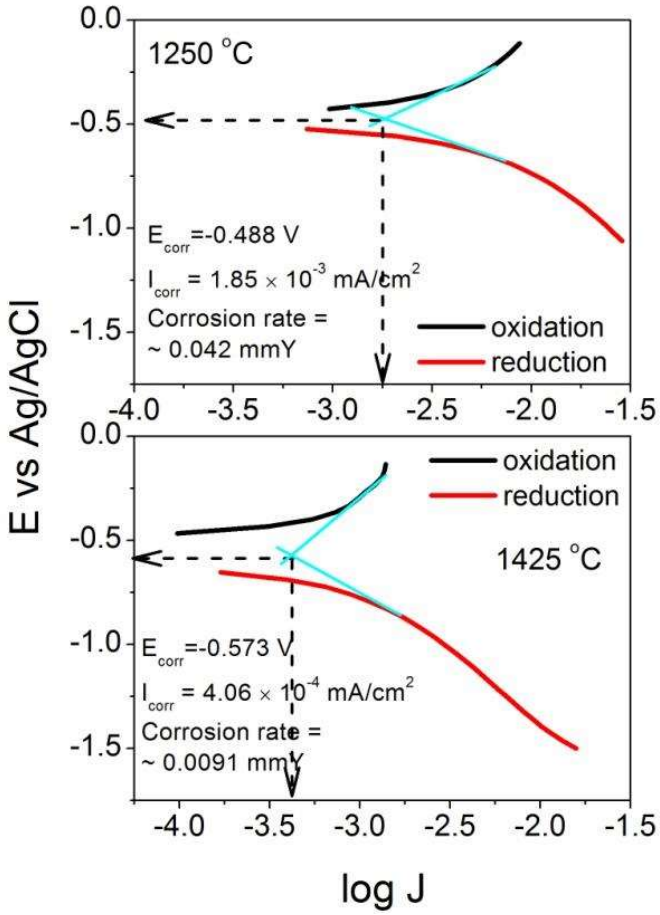

Figure 3.11: Tafel plot showing E_{corr}, I_{corr} and Corrosion rate (CR) of the samples sintered at 1250 °C and 1425 °C (here corrosion rate in mmY stands for mm/year).

3.3.2 Structural Variation after CV

To study the reaction mechanism in the porous and pore-free samples, XRD and FTIR spectroscopy were carried out on the samples after the CV measurements. The different oxide band formations and hydroxyl band groups studied from the FTIR transmission spectra in the pre-CV samples are shown in Fig. 3.12 for all the samples sintered at different sintering temperatures (Fig.3.12(a)). The absorption band at 400 cm^{-1} and range 527-581 cm^{-1} correspond to Ni-O bond. Fig.3.12(b) shows the zoomed part of FTIR spectra in the wavenumber range of 400-700cm^{-1} [148]. It is observed here that 400 cm^{-1} and 527 cm^{-1} modes are complimentary that the intensity corresponding to 400 cm^{-1} increases while intensity

corresponding to 527 cm^{-1} mode decreases. The band at 1000 - 1250 cm^{-1} corresponds to Sm^{3+}-O-Sm^{3+} asymmetric stretching. Moreover, with the increase in sintering temperature, the peak positions corresponding to Sm^{3+}-O and Ni-O are observed to vary, showing the changes in electronic structure due to electronic effects. The bands corresponding to H-O-H observed in the range of 2700 - 4000 cm^{-1}, O-H band corresponding to 1601 - 1615 cm^{-1} are not shifting with the sintering temperature. Rather, their intensities are observed to vary with the increase in sintering temperature. In addition, the intensity of Ni-O band at 400 cm^{-1} is lower in the sample sintered at 1425 ^{o}C in comparison to the sample sintered at 1250 ^{o}C. Simultaneously, the Ni-O band at ~ 500 cm^{-1} has lower intensity in the sample sintered at 1250 ^{o}C in comparison to the sample sintered at 1425 ^{o}C.

Fig. 3.13(a) shows the pre and post effects of CV on the XRD patterns of both samples. It can be observed that the post CV background scattered electron intensity increased in the studied samples. This may be due to a change in the thickness of the samples (lattice expansion after CV, see Fig. 3.13 Table 3.3) with the adsorption of oxygen.

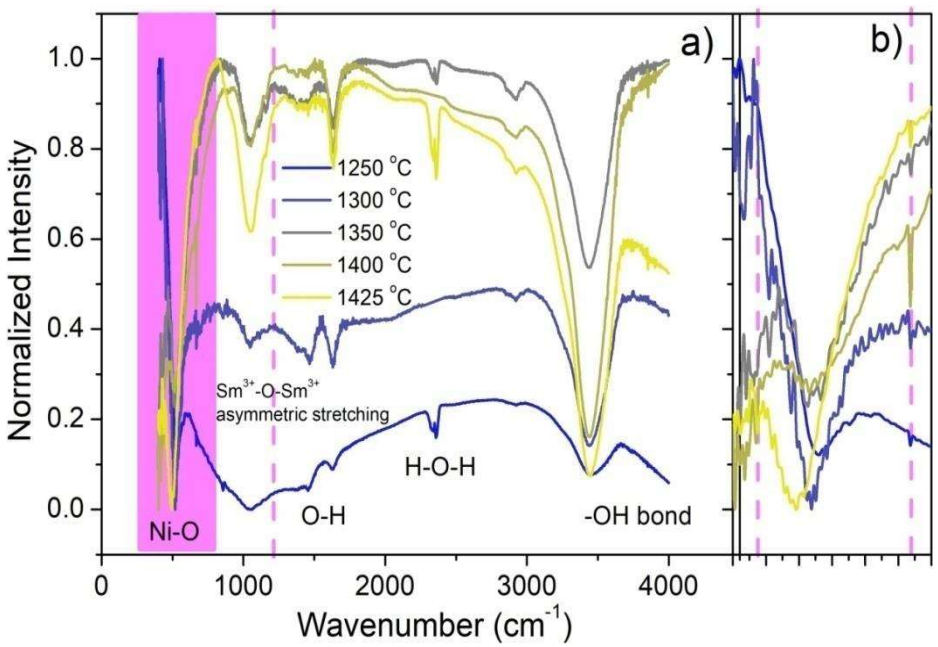

Figure 3.12 (a) The different oxides band formations, hydroxyl band groups, are studied through FTIR transmission spectra of $SmSrNiO_{4-\delta}$ sample sintered at different sintering temperatures (b) FTIR spectra in the range of 400 -700 cm^{-1} for $SmSrNiO_{4-\delta}$ sample sintered at different sintering temperatures.

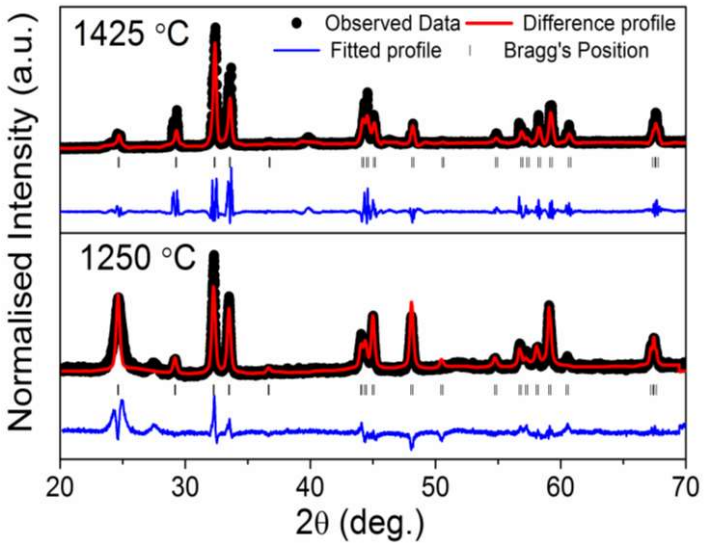

Figure 3.13: Rietveld refined X-ray diffractograms of the $SmSrNiO_{4-\delta}$ sample sintered at 1250 ˚C and 1425 ˚C after cyclic voltammetry.

Sample	Atoms	Position			R-factor			B(Å²)	Lattice Parameters (Å)
		x	y	z	Occupancy	R_{wp}	R_e		
1250	Sm	0	0	0.36375	1	13.7	9.6	0.7341	**a=b= 3.784172**
	Sr	0	0	0.36155	1			0.9704	**c=12.243389**
	Ni	0	0	0	1			0.8332	
	O1	0	0.5	0	1			0.4860	
	O2	0	0	0.17677	1			0.4990	
1425	Sm	0	0	0.35238	1	12.1	7.89	0.7745	**a= b=3.778699**
	Sr	0	0	0.36738	1			0.9872	**c=12.208506**
	Ni	0	0	0	1			0.7876	
	O1	0	0.5	0	1			0.4478	
	O2	0	0	0.16222	1			0.5743	

Table 3.3: Lattice Parameters, atomic positions and Occupancies of $SmSrNiO_{4-\delta}$ composition after Cyclic Voltammetry

In addition to this, after CV, some impurity peaks also appeared, but these were different for both samples. For the porous sample, they indicate the presence of α-$Ni(OH)_2$, while for the pore-free sample, they are likely related to γ- NiOOH. In order to identify these new phases, FTIR analysis for these samples was carried out (Fig. 3.14(b)). The pre-CV FTIR spectrum shows the presence of only hydroxyl band groups above 2000 cm^{-1}. Apart from this, a typical signature for the Ni-O bond is also present in the fingerprint region, particularly the absorption band at ~500 cm^{-1}. However, a sharp change in chemical environment was observed for both samples. The absorption band at ~ 500 cm^{-1} slightly red shifts. The observed red shifts indicates that Ni ion get reduced after CV analysis. The major difference in both samples is the presence of an absorption band at ~ 2900 cm^{-1} (-OH group) for the porous sample and

multiple small absorption bands (shown in grey) between 2000-2500 cm^{-1} (-OOH group) for the pore-free sample[149].

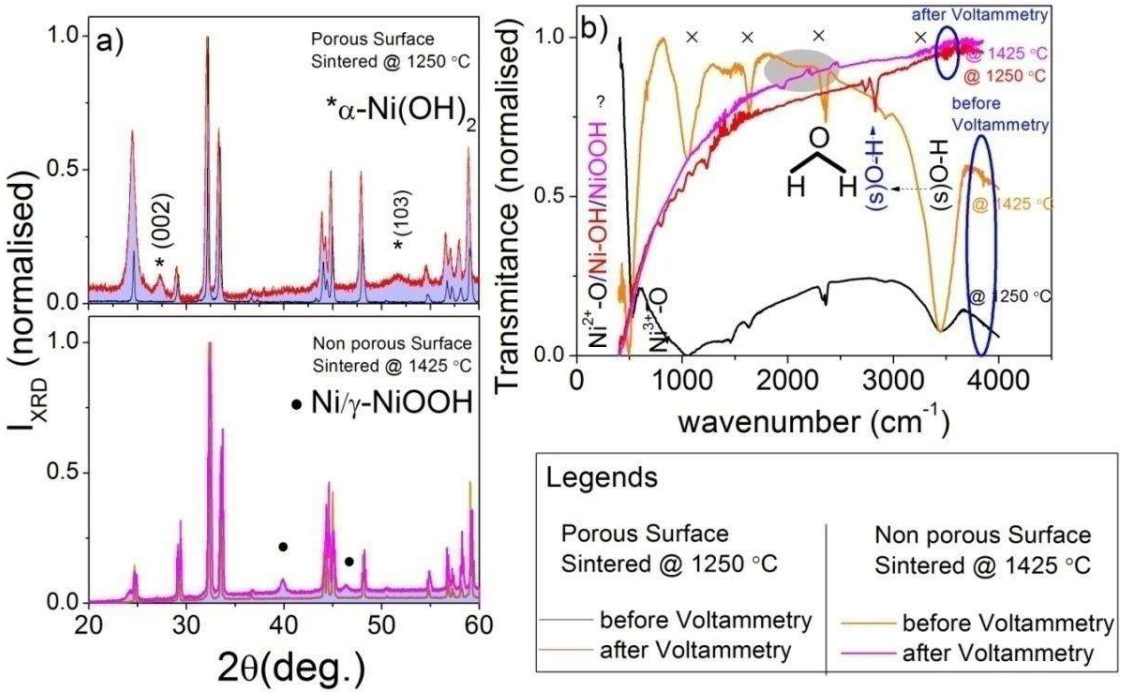

Figure 3.14: A Pre and post effects of CV on the structures of the materials according to the (a) XRD and (b) FTIR of (SmSr)$NiO_{4-\delta}$ sample sintered at 1250 and 1425 °C, respectively

(SmSr)Ni$O_{4-\delta}$ is observed to be a mixed ionic electronic conductor, which is due to the interplay of the Ni-O bond (p-d interactions). P-d interactions play an important role in affecting the properties of magnetic ion containing materials[150]–[152].

In the present case, this interplay is affected by the variation in the sintering temperature, leading to a change from Ni^{3+} to Ni^{2+} through changes in the singly ionized and doubly ionized oxygen vacancies. In the case of octahedral splitting, Ni^{3+} changes to Ni^{2+} upon the addition of electrons into the eg set of orbitals, where the electron intercalation with the redox reaction of the Ni ions leads to alteration of the ion, with bonding occurring between the anion and

intercalated ions, such as Ni and O. In addition, this electron intercalation and addition of oxygen into the interstitial sites shows that there are two different mechanisms upon electrocatalysis. The area under the curve is greater in the CV of the porous sample, showing more oxygen adsorption, which leads to the occurrence of a four-step pathway, resulting in a reduction of OH^- ions and the formation of water.

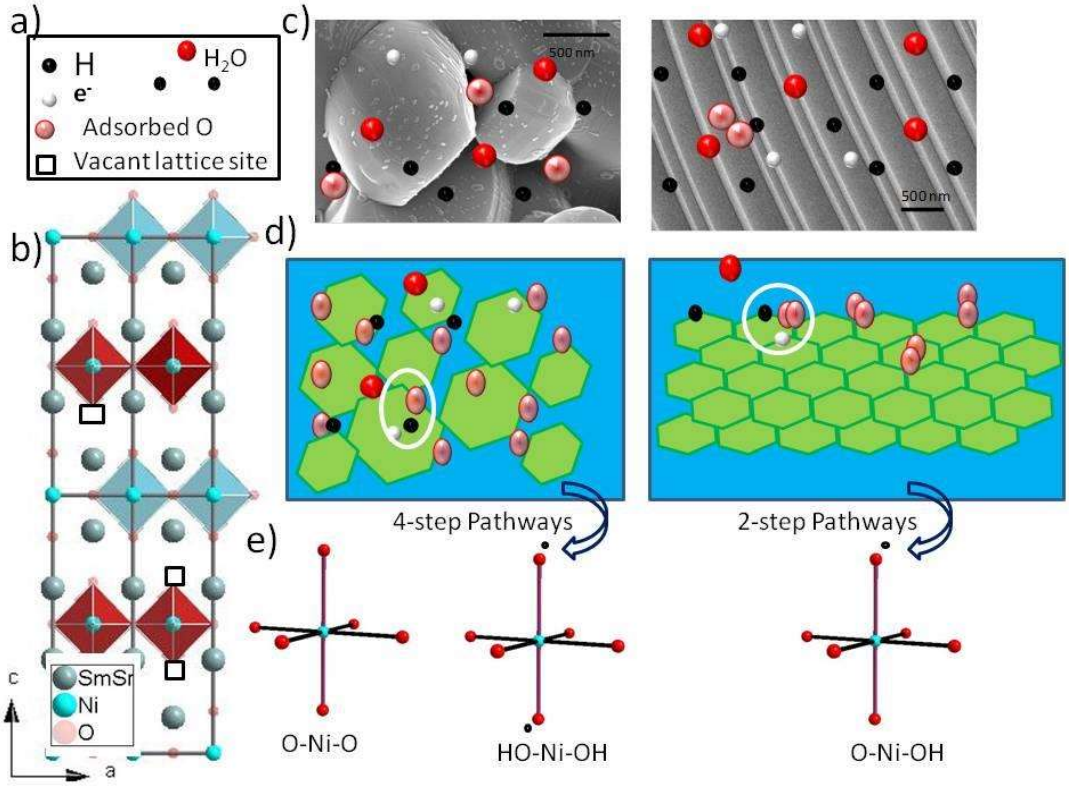

Figure 3.15: (a) Labels of atoms (b) Structure of $(SmSr)NiO_{4-\delta}$ showing the vacant apical oxygens (□) (c) SEM micrographs of porous and pore free samples (d) Surface adsorption mechanism with 4 step and 2 step pathways (e) corresponding alteration in NiO_6 octahedra.

This hydroxyl ion formation leads to the formation of $Ni(OH)_2$, as illustrated in the pathways below. NiOOH formation prevails in the pore-free sample due to the occurrence of meta-stable perhydroxyl ions (OOH^-) *via* a two-step pathway, as shown below. This can also be correlated to the lower area under the curve described earlier, showing that there are pathways with

different number of steps for the two samples with different morphologies. This formation is also depicted in Fig.3.15.

Four-step Pathway[153]:

$$O_2 + \square \rightarrow 2\left(\frac{1}{2}\hat{O}_2\right) \rightarrow 2\hat{O} \quad (3.3)$$

$$\hat{O} + H^+ + e^- \rightarrow \hat{O}H \quad (3.4)$$

$$\hat{O}H + H^+ + e^- \rightarrow H_2\hat{O} \quad (3.5)$$

$$Ni_2O_3 + 2H_2\hat{O} \rightarrow 2Ni(\hat{O}H)_2 + \frac{1}{2}O_2 \uparrow \quad (3.6)$$

Two-step Pathway [152]:

$$O_2 + \square + 2e^- \rightarrow 2\hat{O}^- \quad (3.7)$$

$$\hat{O}_2^- + H^+ + e^- \rightarrow H\hat{O}\,\hat{O}^- \quad (3.8)$$

$$H\hat{O}\,\hat{O}^- + H^+ + e^- \rightarrow H_2O_2 \quad (3.9)$$

$$NiO + H_2O_2 \rightarrow NiOOH + \frac{1}{2}O_2 \uparrow + \frac{1}{2}H_2 \uparrow \quad (3.10)$$

Where $\square$ and $\hat{O}$ represent the vacancies and absorbed oxygen, respectively. Thus, the porous sample undergoes a conduction mechanism *via* a four-step pathway, leading to the formation of H_2O, while the pore-free sample undergoes a mechanism with a two-step pathway, leading to the formation of H_2O_2. H_2O_2 formation is an irreversible reaction and can corrode the material, while H_2O formation is reversible[154]. Hence, the sample sintered at 1425 °C acts as a buffer between the electrode and electrolyte interface while the 1250 °C sintered sample with a higher electronic conductivity is suitable as a cathode.

3.4 Conclusion

Porous and pore-free Ruddlesden-Popper layered structured $(SmSr)NiO_{4-\delta}$ samples were obtained using a conventional solid-state route method at sintering temperatures of 1250 and 1425 ℃, respectively. The pore-free sample is more ionic than the porous sample, while both samples are highly conducting. The electrocatalysis and redox reaction are influenced by the microstructure, altering the surface adsorption mechanism from a four-step pathway (for the porous sample) to a two-step pathway (for the pore-free sample). Conclusively, we propose that the pore-free sample with a higher ionic conductivity and catalytic activity is suitable for use as a buffer layer in between the electrolyte and electrode for solid oxide fuel cells.